RSC Advances

PAPER

View Article Online
View Journal | View Issue

Cite this: *RSC Adv.*, 2018, **8**, 5992

Prussian blue-derived synthesis of uniform nanoflakes-assembled NiS_2 hierarchical microspheres as highly efficient electrocatalysts in dye-sensitized solar cells†

Shoushuang Huang,[a] Haitao Wang,[a] Yang Zhang,[b] Shangdai Wang,[a] Zhiwen Chen,*[a] Zhangjun Hu[a] and Xuefeng Qian*[b]

It's urgent and challenging to explore cost-effective and robust electrocatalyst in the development of large-scaled dye-sensitized solar cells (DSSCs). In this work, we develop a novel strategy to prepare 3D hierarchical NiS_2 microspheres constructed by nanoflakes through a facile chemical etching/anion exchange reaction. Nickel–cobalt Prussian blue analogous (PBA) nanocubes and $(NH_4)_2S$ are employed to initially produce uniform γ-NiOOH/NiS_x hierarchical microspheres, which were then converted to uniform 3D hierarchical NiS_2 microspheres by a controlled annealing treatment. Due to their favorable structural features, the as-obtained NiS_2 hierarchical microspheres possess large surface areas, high structural void porosity and accessible inner surface. All of these advantages facilitate the mass diffusion and charge transport between electrolyte and counter electrode material. As a result, the titled NiS_2 hierarchical microspheres exhibit excellent electrocatalytic activity toward the reduction of I_3^- ions in DSSCs. A typical DSSC with NiS_2 achieves an impressive power conversion efficiency of 8.46% under AM1.5G illumination (100 mW cm^{-2}), higher than that of pyrolysis Pt electrodes (8.04%). Moreover, the fast activity onset and relatively long stability further demonstrate that the NiS_2 hierarchical microspheres are promising alternatives to Pt in DSSCs.

Received 1st January 2018
Accepted 31st January 2018

DOI: 10.1039/c8ra00004b

rsc.li/rsc-advances

1. Introduction

Dye-sensitized solar cells (DSSCs) have received extensive research interest of becoming the third generation solar cells due to their facile fabrication processes, low-cost, and relatively high photoelectric conversion efficiency.[1–3] A typical DSSC consists of a dye-sensitized TiO_2 photoanode, a redox electrolyte containing I_3^-/I^- redox couples, and a counter electrode (CE). As one of the most pivotal components, the CE is responsible for collecting electrons from external circuits and then reducing the I_3^- to I^- ions.[4] Recently, noble metal platinum (Pt) is the most preferred CE electrocatalyst due to its high conductivity and outstanding electrocatalytic activity. However, Pt is of high cost and scarcity and thereby seriously limits its practical application. Additionally, Pt could be easily corroded by iodine-based electrolyte,[5] which would inevitably deteriorate the photovoltaic performance and the long-term stability of DSSCs. Therefore, the development of earth-abundant and active electrocatalyst with high stability is urgently needed to realize the commercial application of DSSCs.

Recently, considerable progress has been achieved on the developments of alternative materials to Pt CE, such as carbon materials,[6–9] conductive polymers,[10,11] metal alloys,[12,13] and transitional-metal compounds.[14,15] Among them, nickel sulfide with a variety of chemical formulas is found to be promising CE material for the I_3^- reduction reaction in DSSCs.[16–19] For example, the hierarchal Ni_3S_4 microspheres reported by Yang *et al.* displayed a power conversion efficiency (PCE) of 6.81% under AM1.5G illumination, comparable to that of Pt-based DSSC (6.85%).[16] Additionally, no obvious degradation of photovoltaic performance was observed in 504 hours, indicating the high stability of nickel sulfide in iodine-based electrolyte. Zheng *et al.* found that both of octahedral and cubic NiS_2 nanocrystals exhibited excellent catalytic activity toward the reduction of I_3^-. The corresponding DSSCs with octahedral NiS_2 and cubic NiS_2 achieved a high PCE of 5.98% and 5.43%, respectively.[20] The well-defined NiS/Ni_3S_2 nanorod composite array prepared by Pan's group also manifested a high catalytic activity for the regeneration of I_3^- ions, and attained comparable photovoltaic performances with Pt CE.[21] These extraordinary electrochemical performance of DSSCs depends on the

[a]School of Environmental and Chemical Engineering, Shanghai University, Shanghai 200444, China. E-mail: zwchen@shu.edu.cn

[b]Shanghai Electrochemical Energy Devices Research Center, School of Chemistry and Chemical Engineering, State Key Laboratory of Metal Matrix Composites, Shanghai Jiao Tong University, Shanghai 200240, China

† Electronic supplementary information (ESI) available. See DOI: 10.1039/c8ra00004b

fascinating morphologies, rich redox reactions, and diverse photoelectric properties of nickel sulfide CEs. Therefore, taking into consideration the high earth abundance, the superior catalytic activity and the excellent chemical stability, nickel sulfide is a promising CE candidate for the large-scale manufacture of low-cost DSSCs.

It's well known that the architecture is one of the key factors in the determination of electrochemical performance of electrode materials. Recently, two-dimensional (2D) nanomaterial has been considered as one kind of ideal morphological foundation for the surface-dependent electrochemical reactions due to the high percentages of surface atoms, abundant active sites and high exposures of low-energy facets.[22,23] However, the major problem associated with the application of 2D materials in catalysis lies in their insufficient number of internal spaces caused by their direct and free accumulation on devices.[24] In contrast, 3D hierarchical architectures provide the potential of combining the merits of low-dimensional material in a single structure, such as higher surface/volume ratio, larger porosity and accessible interior space.[25] These characteristics can facilitate the filling and diffusion of electrolyte, shorten the diffusion distance as well as increase the catalytic active sites, which are important to boost the photovoltaic performances of DSSCs. On the basis of the above investigations, it seems logical to envision that 3D hierarchical NiS_2 architectures constructed by 2D building blocks can be favorable for constructing high performance of DSSCs. Up to now, typical strategy for fabricating NiS_2 superstructures is template-engaged synthesis.[26–28] Therefore, the fabrication of 3D hierarchical NiS_2 superstructures using simple wet chemical methods under mild conditions is still relatively challenging.

Recently, chemical etching has been regarded as an efficient method to prepare complex nanostructures with unique physicochemical properties, and a series of high-quality metal oxides/sulfides complex nanostructure have been successfully fabricated by selective etching of Prussian blue analogues (PBA).[29–31] Inspired by them, in the present work, nanoflakes-assembled NiS_2 hierarchical microspheres were synthesized through a facile chemical etching/anion exchange reaction. Nickel–cobalt Prussian blue analogous (PBA) nanocubes and $(NH_4)_2S$ are employed to initially produce uniform γ-NiOOH/NiS_x hierarchical microspheres, which are then converted to uniform 3D hierarchical NiS_2 microspheres *via* a controlled annealing treatment. The as-obtained NiS_2 hierarchical microspheres combine the merits of 2D and 3D materials when employed as CE catalysts in DSSCs: (1) the 2D nanoflakes provide larger electrochemical active sites and shorter electron diffusion path to catalyze the reduction of I_3^-. (2) The 3D hierarchical architectures offer a higher surface/volume ratio, larger porosity and accessible inner surface to facilitate the diffusion of electrolyte. (3) The 3D hierarchical structures provide wide spaces for acetylene black filling in and make the microspheres contact more efficiently to conductive substrate, which helps to reduce the resistance of devices. As a result, the NiS_2 hierarchical microspheres exhibited low charge transfer resistance at the electrolyte–electrode interface, high electrocatalytic activity and fast reaction kinetics for the I^-/I_3^- redox reaction.

2. Experiment section

2.1 Synthesis of NiCo PBA nanocubes

The NiCo PBA nanocubes were synthesized through a previously reported method with slight modification.[32] In brief, 3.0 mmol of $Ni(NO_3)\cdot 6H_2O$ and 4.5 mmol of $Na_3C_6H_5O_7\cdot 2H_2O$ were dissolved in 100 mL of deionized water under vigorous stirring to form a clear solution. Then, this green solution was rapidly injected into 100 mL of aqueous solution containing 2.0 mmol of $K_3[Co(CN)_6]$. The obtained mixed solution was allowed to age for 24 h at room temperature. Finally, the product was collected by centrifugation and washed with water and ethanol for several times, and dried at 80 °C in a vacuum oven for 12 h.

2.2 Synthesis of 3D hierarchical NiS_2 microspheres

In a typical synthesis, 60 mg of the above as-prepared NiCo PBA nanocubes were dispersed into 60 mL of ethanol to form a homogeneous suspension with the assistance of ultrasonication for 30 min. At the meantime, 3.0 mL $(NH_4)_2S$ ($\geq$8.0%) aqueous solution was dissolved into 30 mL of deionized water. The $(NH_4)_2S$ solution was then poured into the above NiCo PBA suspension under magnetic stirring for 30 min. Finally, the resulting mixture was transferred into a Teflon-lined stainless-steel autoclave and kept at 100 °C for 10 hours in an electric oven. The final products were collected by centrifugation, and washed with water and ethanol before drying at 80 °C overnight. Then, 30 mg of the as-obtained sample was placed at the downstream side of crucible, and 120 mg of sublimed sulfur powder was placed at the upstream side of the crucible. The crucible was subsequently placed into the tube furnace and calcined under nitrogen atmosphere at 350 °C for 2 hours with a ramp rate of 2 °C min^{-1}. After cooling down to room temperature, 3D NiS_2 hierarchical microspheres were obtained.

2.3 Preparation of counter electrodes

CEs were prepared by a slurry coating procedure on the cleaned FTO substrates. The slurry was prepared by mixing 80 mg of NiS_2 catalyst, 10 mg of acetylene black and 10 mg of polyvinylidene fluoride into 1.0 mL *N*-methyl-2-pyrrolidone followed by sonication for 30 min to form a homogeneous ink. The resulting slurry was then coated onto the FTO substrate using a doctor blade method. The area of active layer was masked by the transparent adhesive tape layers tape with an aperture area of 0.5 × 0.5 cm^2, and the thickness of the CE film was strictly controlled to be 4 μm. Finally, the electrodes were dried at 60 °C for 12 hours in a vacuum oven. For comparison, pyrolytic Pt CE was prepared by drop-casting 50 μL of H_2PtCl_6 in ethanol (5 mM) on a 1.5 × 1.5 cm^2 FTO glass followed by sintering at 400 °C for 30 min.

2.4 Fabrication of DSSCs

The commercial TiO_2 photoanodes (Ying kou Opvtech New Energy Co., Ltd) were first annealed at 500 °C for 1 hour. After being cooled down to 80 °C, the TiO_2 photoanodes were immersed in a 0.5 mM ethanol solution of N719 dye (Solaronix

SA, Switzerland) for 20 h. DSSCs were fabricated by assembling the N719-sensitized TiO_2 photoanodes and CEs with a hot-melt film as spacer (Surlyn 1702; DuPont, 60 μm in thickness). The cell internal space was filled with electrolyte using a vacuum pump followed by a sealing procedure with a Surlyn film and a cover glass under heating. The liquid electrolyte was composed of 0.60 M 1-butyl-3-methylimi-dazolium iodide, 0.03 M I_2, 0.50 M 4-*tert*-butyl pyridine, 0.06 M lithium iodide and 0.10 M guanidinium thiocyanate of anhydrous acetonitrile. The sealed DSSCs were used for the photocurrent–voltage test with an active area of 0.16 cm^2.

2.5 Characterization

The phase and crystal structure of the as-obtained products was characterized by powder X-ray diffraction (XRD) (Shimadzu XRD-6000) with Cu Kα radiation. The morphologies and crystal lattice of the samples were characterized by field-emission scanning electron microscopy (FESEM, JEOL, JSM-6700F) and high-resolution transmission electron microscopy (HRTEM, JEOL, JEM-2100F), respectively. The X-ray photoelectron spectroscopy (XPS) analysis was performed on a VG Scientific ESCLAB 220iXL X-ray photoelectron spectrometer with Al Kα (1486.6 eV) as the X-ray source. The surface area and porosity of the materials was analyzed by using a NOVA 2200e instrument. The photocurrent–voltage tests of DSSCs were performed under AM 1.5 illumination (100 mW cm^{-2}) in ambient condition on a 94023A Oriel sol3A solar simulator (Newport) with 450 W xenon lamp as light source. Electrochemical impedance spectroscopy (EIS) experiments and Tafel-polarization curves were measured with dummy cells in the dark by using a Zahner electrochemical workstation (Zahner Zennium CIMPS-1, Germany). The frequency range of EIS experiments was from 100 mHz to 1 MHz with an AC modulation signal of 10 mV and bias DC voltage of 0 V. The resultant impedance spectra were analyzed *via* the Z-view software. Tafel-polarization measurements were carried out with a scan rate of 5 mV s^{-1}. Cyclic voltammetry was conducted in a three-electrode system in an acetonitrile solution of 0.1 mmol $LiClO_4$, 10 mmol LiI and 1 mmol I_2 at a scan rate of 50 mV s^{-1}. Platinum nets electrode served as a CE, and the Ag/AgCl couple was used as a reference electrode.

3. Results and discussion

Field emission scanning electron microscopy (FESEM) images showed that the as-prepared $Ni_3[Co(CN)_6]_2$ PBA nanocubes had a highly uniform and well-defined cubic structure with an average size of 242 nm (Fig. 1a and b), and the corresponding transmission electron microscopy (TEM) image indicated these PBA nanocubes presented a solid and dense texture (Fig. 1c). The NiCo PBA nanocubes were then employed as nickel source to react with $(NH_4)_2S$ aqueous solution at 100 °C for 10 hours. FESEM images clearly revealed that the as-obtained product was composed of uniform and monodispersed microspheres with an average diameter of 2.0 μm (Fig. 1d). An enlarged SEM image indicated that each microsphere was constructed by 2D

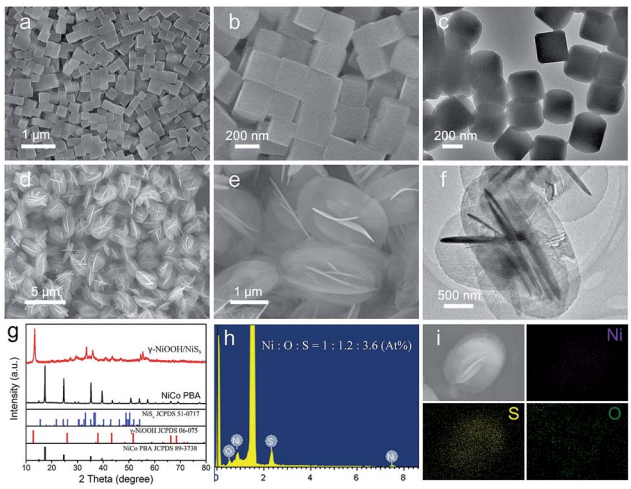

Fig. 1 SEM (a, b, d, e) and TEM (c, f) images of the as-prepared NiCo PBA nanocubes (a–c) and γ-NiOOH/NiS_x (d–f) microspheres; XRD patterns (g), EDX spectrum (h) and element mapping (i) of the γ-NiOOH/NiS_x hierarchal microspheres.

nanoflakes building blocks in self-assemble style (Fig. 1e). The thickness of the nanoflake was in the range of 17–28 nm determined by TEM image (Fig. 1f). Fig. 1g showed the X-ray diffraction pattern (XRD) of the as-synthesized sample. The crystallographic phase of the product could be identified as γ-NiOOH (JCPDS 06-075) and NiS_x (JCPDS, 51-0717), respectively. Energy dispersive X-ray spectroscopy (EDX) showed the Ni : O : S atomic ratio to be 1 : 1.2 : 3.6 (Fig. 1h), and the corresponding elemental mapping images indicated that these elements were uniformly distributed in a single microsphere (Fig. 1i). From the results mentioned above, we concluded that the as-obtained product was composed of γ-NiOOH and NiS_x.

In the present synthesis strategy, the NiCo PBA nanocubes as nickel source was critical for the formation of uniform 3D hierarchical γ-NiOOH/NiS_x microspheres. Replacing NiCo PBA nanocubes with nickel nitrate or nickel acetate while keeping the other synthesis parameters similar, irregular nano/micro-sized nickel sulfide particles with large size-distribution were obtained (Fig. S1†). This result can be explained by the fact that the excessively release of Ni^{2+} cations from metal salts lead to the fast nucleation and growth of nickel sulfides.[33] Further study indicated that the formation of uniform γ-NiOOH/NiS_x hierarchical microspheres also depended upon reaction temperature. When the reaction temperature was over 140 °C, NiS_2 nanoparticles (NPs) with average size of ~200 nm were obtained (Fig. S2†). In contrast, nearly no product could be obtained when the reaction was carried out at room temperature. The above findings demonstrated that the precise control over reaction rate was crucial for the formation of high-quantity γ-NiOOH/NiS_x hierarchical microspheres.[29] Therefore, a proper amount of ethanol was introduced into the reaction system to slow down the etching of NiCo PBA nanocubes as well as the nucleation of nickel sulfides (Fig. S3†).

To investigate the structural evolution from NiCo PBA nanocubes to the γ-NiOOH/NiS_x hierarchical nanostructures, a series of experiments with different reaction times were

conducted. In order to further slow down the reaction rate, the reaction were carried out in 90 mL ethanol and 10 mL H_2O. The structure and morphologies of the intermediate products collected at different reaction stages were shown in Fig. 2. After a reaction time of 0.5 hour, the edges of the NiCo PBA nanocubes were etched, while their plane surfaces remained unchanged (Fig. 2b and c). This phenomenon indicated the different reaction activity between the edge and plane parts, which is in good agreement with Yu's report.[29,31] When the reaction was carried out for 1.0 hour, the NiCo PBA nanocubes disappeared and thin nanoflakes were observed (Fig. 2d). This nanoflakes were identified mainly to be γ-NiOOH by XRD (Fig. S4†). At a longer reaction time of 10 hours, the nanoflakes were connected with each other and self-assembled into uniform hierarchical microspheres (Fig. 2e).

Based on the experimental results mentioned above, a possible growth mechanism for the γ-NiOOH/NiS_x hierarchical microspheres was proposed. The double hydrolysiss of $(NH_4)_2S$ produced $NH_3 \cdot H_2O$ and H_2S gas in solution, which were further hydrolyzed to hydroxide ion (OH^-) and polysulfide ions (S_x^{2-}).[34] Thus, the NiCo PBA nanocubes were easily etched by these species. As more defects were existed on the rough edges, the etching reaction preferentially took place on the edges of NiCo PBA nanocubes.[29] In this way, γ-NiOOH was easily formed due to the reaction between Ni^{2+} and OH^- ions. At the same time, the γ-NiOOH transition continuously converted into NiS_x driven by the thermodynamic equilibrium due to the larger solubility product constant of hydroxides compared with sulfide (Fig. S4†). The EDX spectra showed the decrease of oxygen content and the increase of sulfur content as the reaction proceeds, evidencing the anion exchange between OH^- and S^{2-} (Fig. S5†). Similar phenomenon has been observed for many other transition metal hydroxides by matching the solubility product of their hydroxides and sulfides.[35,36]

Recently, many transition metal hydroxides have been utilized as precursors to prepare novel functional chalcogenides with satisfied performance. Herein, we converted the γ-NiOOH/NiS_x microspheres to nickel sulfides *via* thermal decomposition and sulfuration reaction. As shown in Fig. 3a, all of the diffraction peaks were well indexed to cubic NiS_2 (JCPDS 65-3325, $Pa\bar{3}$, $a = b = c = 5.678$ Å). No peaks from other crystalline

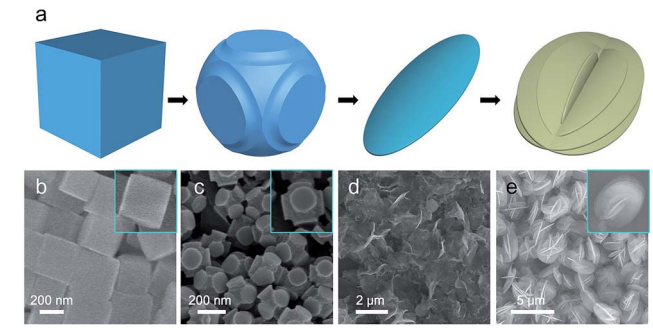

Fig. 2 Schematic illustration of the formation process of γ-NiOOH/NiS_x hierarchical microspheres (a). FESEM images of the products obtained after reaction for (b) 0 hour, (c) 0.5 h, (d) 1.0 hour, and (e) 10 hour.

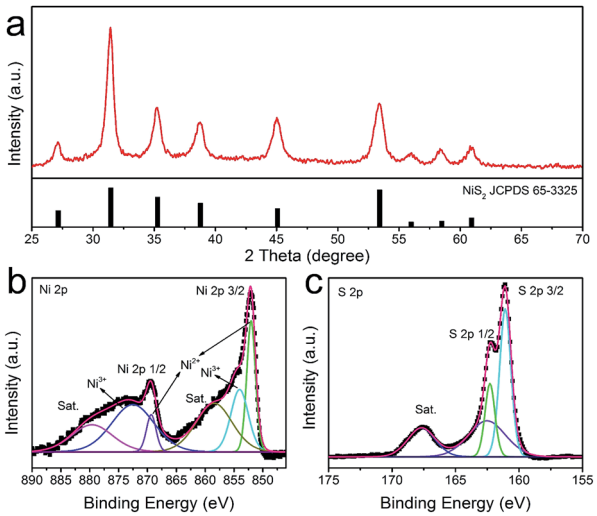

Fig. 3 XRD (a) and XPS spectrum of the as-prepared NiS_2 hierarchical microspheres: (b) Ni 2p and (c) S 2p.

byproducts could be identified, indicating the hydroxides phase was completely decomposed and converted into metal sulfide. X-ray photoelectron spectroscopy (XPS) was further used to analyze the valence state and the surface composition of the as-obtained product. By using a Gaussian fitting method, the Ni 2p spectrum can be deconvoluted into two spin orbit doublets and two shakeup satellites (identified as "Sat.") (Fig. 3b). It was found that the strong peaks at the binding energies of 851.9 and 869.4 eV could be attributed to 2p3/2 and 2p1/2 of Ni^{2+} species, and the peaks at 854.1 and 872.5 eV could be assigned to 2p3/2 and 2p1/2 of Ni^{3+} species, respectively.[37] The existence of Ni^{3+} indicated the slight surface oxidation state of the sample, which was consistent with previous reports.[38] The XPS spectrum of S 2p was shown in Fig. 3c. The peaks at 161.1 and 162.3 eV were associated with S 2p3/2 and S 2p1/2, respectively. Similarly, the minor peak near 162.5 eV suggested the presence of higher oxidation state sulfide species in the sample.[39] The XPS results were in agreement with XRD, confirming that the as-obtained sample was indeed composed of pure NiS_2.

The morphology details of the annealed sample was then investigated by SEM and TEM. As one can see in Fig. 4a, the hierarchical structure was basically maintained after calcination. However, the nanoflakes of the NiS_2 microspheres became porous with rough surfaces in contrast to the smooth surfaces of the hydroxides precursor (Fig. 4b). A typical TEM image in Fig. 4c indicated the nanoflake was composed of nanocrystals with size of several nanometers. The lattice fringes were clearly displayed in a high-resolution TEM image and the interplanar spacing of 2.83 Å and 2.53 Å could be ascribed to the (200) and (210) planes of cubic-phase NiS_2, respectively (Fig. 4d). The selected area electron diffraction (SAED) confirmed the polycrystalline nature of the annealed sample (Fig. 4e). In virtue of the 3D hierarchal structure, the NiS_2 microspheres possessed a relatively high Brunauer–Emmett–Teller (BET) surface area of about 69.8 $m^2\ g^{-1}$ (Fig. S6†). It's clear that this hierarchical structure is beneficial for mass transport and fast diffusion of the electrolyte during the electrocatalysis process.

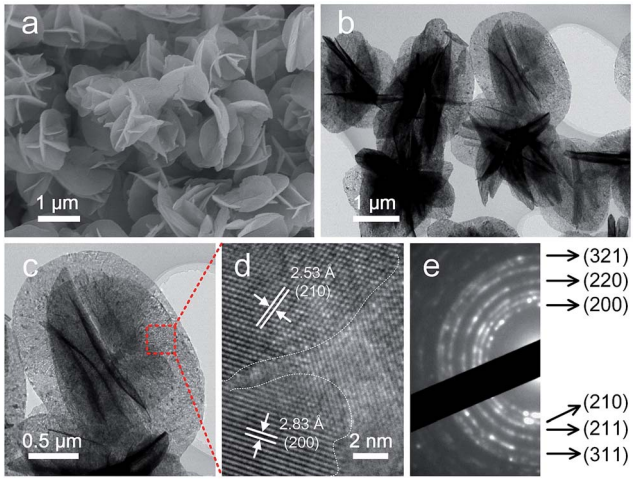

Fig. 4 SEM (a), TEM (b, c), HRTEM (d) images and SAED pattern (e) of the as-obtained NiS_2 microspheres after annealing at 350 °C for 2 hours under nitrogen atmosphere.

Sandwich-structure devices were assembled to assess the potential application of NiS_2 hierarchical microspheres in DSSCs. The current density–voltage (J–V) curves were shown in Fig. 5a and the related photovoltaic parameters including short circuit current density (J_{sc}), open circuit voltage (V_{oc}), power conversion efficiency (PCE) and fill factor (FF), were summarized in Table 1 and S1.† The DSSC with NiS_2 microspheres (MSs) CE produced a V_{oc} of 746 mV, a J_{sc} of 16.23 mA cm^{-2} and a FF of 0.70, thus yielding an overall PCE of 8.48%. This was an improved photovoltaic performance compared to that of the device employing Pt CE (V_{oc} = 761 mV, J_{sc} = 15.86 mA cm^{-2}, FF = 0.65, η = 7.84%). Comparing these parameters, we can find that the enhancement of PCE was mainly contributed by the improvement of J_{sc} and FF. The increased J_{sc} can be attributed to the accelerated reduction of I_3^- ions by NiS_2 microspheres, which subsequently resulted in the fast regeneration of N719 molecules.[40] The improvement of FF corresponded to the reduced charge-transfer resistance at the CE/electrolyte interface and diffusion resistance of I_3^- in the electrolyte. Additionally, to demonstrate the structural advantage of 3D hierarchical structures in catalysis, the obtained irregular NiS_2 nanoparticles (NPs) were also used as CE catalyst for comparison. It was found that the performance of the device with NiS_2 NPs CE was significantly inferior to those with NiS_2 MSs and Pt CEs. This observation demonstrated the higher catalytic activity of 3D nanostructure based CEs due to the numerous catalytic active sites exposed on the surface. These results were also supported by the IPCE measurement, in which the NiS_2 MSs based device exhibited a highest efficiency than the other two CEs (Fig. 5b). The IPCE followed the same trend with the difference of PCE and J_{sc} values, confirming the as-prepared NiS_2 hierarchical microspheres CE could provide sufficient and fast regeneration of I_3^- ions in the electrolyte.[41]

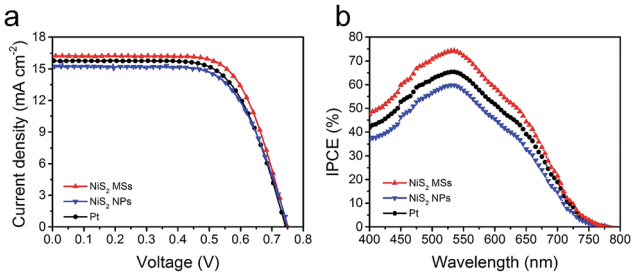

Fig. 5 J–V cures (a) and IPCE spectrum (b) of the DSSCs using NiS_2 MSs, NiS_2 NPs and Pt CEs, measured at AM1.5G illumination.

Table 1 Photovoltaic performance of DSSCs with various CEs under AM1.5G illumination (100 mW cm^{-2})

CEs	V_{oc} (mV)	J_{sc} (mA cm^{-2})	FF	PCE (%)
NiS_2 MSs	745 ± 3.77	16.28 ± 0.04	0.70 ± 0.01	8.46 ± 0.06
NiS_2 NPs	745 ± 2.16	15.27 ± 0.03	0.68 ± 0.00	7.76 ± 0.04
Pt	741 ± 3.87	15.66 ± 0.11	0.69 ± 0.01	8.04 ± 0.05

To evaluate the electrocatalytic activities of the as-prepared CEs toward the reduction of I_3^- ions, cyclic voltammetry (CV) measurements were carried out in a three-electrode system. As shown in Fig. 6a, all electrodes exhibited two typical pairs of oxidation–reduction peaks, suggesting that the NiS_2 CEs can exhibit Pt-like electrocatalytic behavior. The left peak in low potential range is assigned to the oxidation (Ox-1) and reduction (Red-1) of I^-/I_3^-, and the right one in high potential range corresponds to the oxidation (Ox-2) and reduction (Red-2) of I_2/I_3^-.[42] The peak current density of Red-A and peak-to-peak separation (E_{pp}) between Red-1 and Ox-1 are the two important parameters for evaluating the catalytic activities of different CEs.[43] The NiS_2 MSs CE produced a higher peak current density (1.76 mA cm^{-2}) than that of NiS_2 NPs (1.48 mA cm^{-2}) and Pt CE (1.63 mA cm^{-2}), indicating it had better electrocatalytic activity for the reduction of I_3^- ions. Additionally, the E_{pp} of NiS_2 MPs CE (330 mV) was also smaller than those of NiS_2 NPs (482 mV) and Pt CE (343 mV), which suggested a smaller overpotential for the reduction reaction on NiS_2 MSs CE.[44] The higher peak current density and lower E_{pp} value indicated the NiS_2 MSs CE presented higher catalytic activity for the reduction of I_3^- to I^-. The excellent catalytic activity of NiS_2 MPs CE can be attributed to its large active surface area and abundant hierarchical pore structure, which provided more catalytic activity sites and the higher charge transfer rate. Additionally, the stacking CV plots of NiS_2 MPs CE were recorded at a scan rate from 10 to 150 mV s^{-1} (Fig. S7†). The good linear relationships between the peak current density and the square root of corresponding scan rate implied the reduction process of I^-/I_3^- redox couples at NiS_2 CE obeyed a diffusion-controlled mechanism, and there was no specific interactions between NiS_2 CE and I^-/I_3^- redox couples.[45]

Electrochemical impedance spectroscopy (EIS) measurements were further used to investigate the internal resistance and charge transfer kinetics at the CE/electrolyte interface. The Nyquist plots for symmetric cells (CE/electrolyte/CE) were shown in Fig. 6b and the fitted results were listed in Table 2. The intercept on the real axis can be assigned to the ohmic series

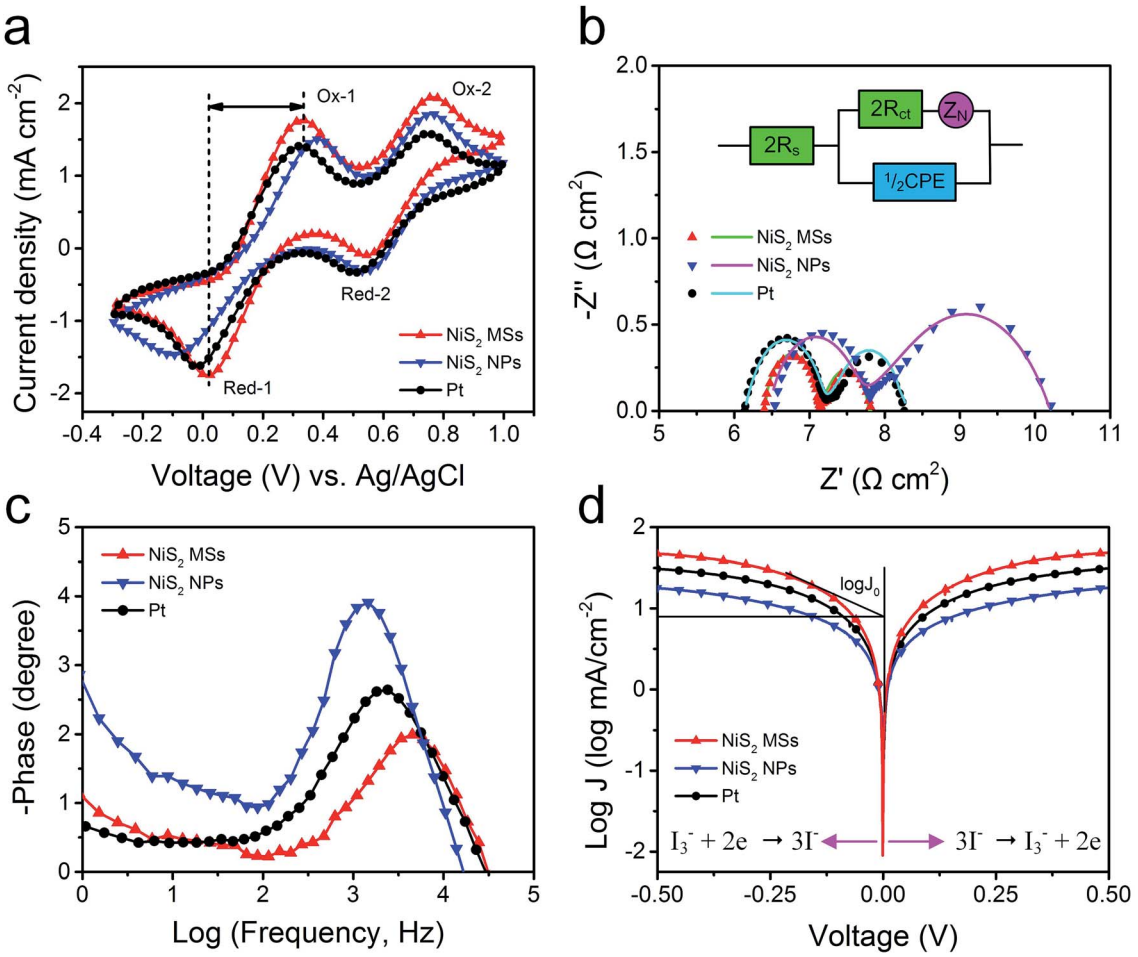

Fig. 6 (a) Cyclic voltammograms measured in an iodine-based electrolyte with a scanning rate of 50 mV s^{-1}. (b) Nyquist and (c) Bode EIS plots, and (d) Tafel polarization curves for the symmetric dummy cells fabricated by two identical CEs. The inset shows an equivalent circuit simulated by Z-view software.

Table 2 The electrochemical parameters for different CEs

CEs	R_s (Ω cm^2)	R_{ct} (Ω cm^2)	CPE-T (μF cm^{-2})	CPE-P	$W_s - R$ (Ω cm^2)	$W_s - T$	$W_s - P$	τ (μs)	E_{pp} (mV)
NiS_2 MSs	3.23	0.37	259.2	0.81	0.68	0.011	0.50	31.7	330
NiS_2 NPs	3.27	0.63	96.4	0.93	2.44	0.005	0.50	116.9	482
Pt	3.09	0.55	71.6	0.88	1.08	0.015	0.50	71.4	343

resistance (R_s). The semicircles in frequency regions between 1 kHz and 100 kHz can be attributed to the resistance capacitance of the electrode/electrolyte interface, including the charge transfer resistance (R_{ct}) and the corresponding double-layer capacitance (C_μ). The arc at low frequency regions can be assigned to the Warburg impedance (W_s) in the electrolyte.[46] Typically, R_{ct} is regarded as an indicator to reveal the charge transfer process and thereby to evaluate the catalytic activity of catalysts. Constant phase element (CPE) is frequently used as a substitute for a capacitor in anequivalent circuit to fit the impedance behavior of the electrical double layer, which can be defined as: $\mathrm{CPE} = (\text{CPE-T})^{-1}(j\omega)^{-(\text{CPE-P})}$, where $j^2 = -1$, ω is the frequency and CPE-T, CPE-P are the frequency-independent parameters of the CPE.[47,48] Generally, a larger CPE-T means an increase in the active surface area, and a decrease of CPE-P means an increase in the porosity. Additionally, the Warburg impedance equals: $W_s = R\tanh([j\omega T]^P)(j\omega T)^{-P}$, in which $P = 0.5$, R is the diffusion impedance and T is the relationship of the effective diffusion thickness and the effective diffusion coefficient.[49] These electrochemical parameters can be obtained by fitting EIS spectra using a Z-view software.

The NiS_2 CEs yielded similar R_s value with Pt CE due to the addition of acetylene black, hence posing similar influence on the photovoltaic performances. The simulated R_{ct} value of NiS_2 MSs CE was 0.37 Ω cm^2, smaller than those of NiS_2 NPs (0.63 Ω cm^2) and Pt CE (0.55 Ω cm^2), which suggested that the

NiS_2 MSs CE had better electrocatalytic activity for the reduction of I_3^- ions. The simulated CPE-T values were 96.4 μF cm^{-2} for Pt CE and 71.6 μF cm^{-2} for NiS_2 NPs CE, both of which were much lower than the value of 259.2 μF cm^{-2} obtained for the NiS_2 MSs CE. These results demonstrated the NiS_2 MSs CE had larger specific surface area and the higher electrolyte penetration in the hierarchical microstructure.[50] In addition, the diffusion impedance for the symmetric cells increased by a sequence of NiS_2 MSs (0.68 Ω cm^2) < Pt (1.08 Ω cm^2) < NiS_2 NPs (2.44 Ω cm^2), revealing a faster diffusion velocity of the redox species in the electrolyte for NiS_2 MSs CE. The main role of CE is to reduce the I_3^- to I^-, thus, the actual lifetimes of electrons (τ) participating in the I_3^- reduction reaction can also be used to evaluate the catalytic activity of different CEs, which can be calculated according to formula:[51] $\tau = 1/2\pi f_p$, in which f_p is the peak of the high-frequency region in the Bode spectra (Fig. 6c). The order of the calculated τ value is 31.7 μs (NiS_2 MSs) < 71.4 μs (Pt) < 116.9 μs (NiS_2 NPs). Apparently, the shorter lifetime in NiS_2 MSs CE implied it had higher electrocatalytic activity for the reduction of I_3^- ions than that of Pt CE, which was consistent with the results derived from the CV data and photovoltaic parameters.

EIS analysis of complete DSSCs were further studied under light illumination of 100 mW cm^{-2} in the frequency range of 0.1 Hz to 100 kHz using an applied bias of V_{oc} (Fig. S8†). The charge transport impedances (R_t) at the CE/electrolyte interface for various CEs were higher than those measured with symmetric cells, but the value for NiS_2 MSs CE (0.84 Ω cm^2) was still smaller than the Pt (1.12 Ω cm^2) and NiS_2 NPs (1.39 Ω cm^2) CEs. This result confirmed the NiS_2 MSs CE has the best electrocatalytic activity for the reduction of I_3^-. Additionally, CPE magnitude of CE (CPE) increased in the order of NiS_2 NPs (52.15 mF cm^{-2}) < Pt (144.42 mF cm^{-2}) < NiS_2 MSs (278.80 mF cm^{-2}), suggesting a same order of the active surface area. The conclusions for the catalytic activity derived from the EIS data with symmetric dummy cells and complete DSSCs were consistent.

To further examine the interfacial charge-transfer behaviors of the I_3^-/I^- couple on CE surface, Tafel polarization measurements were carried out on the symmetric cells used in the EIS experiments. Tafel curve can be divided into three zones depending on the overpotential value: the polarization zone at low overpotential ($|V|$ < 120 mV), Tafel zone at intermediate overpotential (with a sharp slope), and diffusion zone at high overpotential. In the Tafel zone, the intersection of the cathodic branch and the equilibrium potential line can be regarded as J_0, which can be obtained by extending the line to zero voltage and measuring the intercept on the J-axis (y-axis). As shown in Fig. 6d, the slope of a tangent for NiS_2 MSs CE was slightly higher than that of NiS_2 NPs and Pt CE, implying the NiS_2 MSs CE had larger exchange current densities and thereby better catalytic activity. The J_0 value can also be calculated from the formula:[52] $J_0 = RT/nFR_{ct}$, where R is the gas constant, T is the absolute temperature, F is Faraday's constant and R_{ct} is charge transfer resistance obtained from EIS plots. The order of the calculated R_{ct} values was NiS_2 MSs < Pt < NiS_2 NPs, which was consistent with the results from the EIS analysis. In the diffusion zone, the intersection of the cathodic branch with the y-axis can be regarded as limited current density (J_{lim}), a parameter depending on the diffusion coefficient (D_n) of the redox couple in electrolyte. The larger intersection of the cathodic branch with the y-axis demonstrated the NiS_2 MSs CE had higher limited current density (J_{lim}) and higher diffusion velocity.[53]

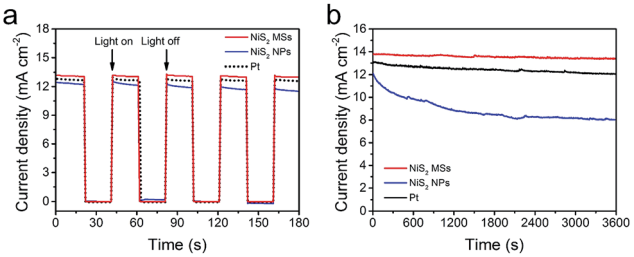

Fig. 7 Start-stop switches (a) and photocurrent stabilities (b) of the DSSCs using NiS_2 MSs and Pt CEs. The on–off plots are achieved by alternately irradiating (100 mW cm^{-2}) and darkening (0 mW cm^{-2}) the DSSC at 0 V, whereas the photocurrent stabilities are carried out under a sustained irradiation of 100 mW cm^{-2}.

Fig. 7a showed the start/stop switching of the DSSCs with NiS_2 MSs and Pt CEs at alternatively on/off illumination. The abrupt increase in photocurrent density without delay in starting the cell indicated that both of NiS_2 MSs and Pt CEs were vigorous in catalyzing the reduction of I_3^- ions.[13] However, only 67.5% and 92.1% of the initial photocurrent density was remained for the device with NiS_2 MSs and Pt CEs under persistent irradiation for 3600 s under illumination at 100 mW cm^{-2}, in comparison to 97.2% for NiS_2 MSs based DSSC (Fig. 7b). This result indicated that NiS_2 MSs CE had better stability. In order to cross-check the stability, the two CEs were subjected to sequential scanning CVs for 100 cycles at a scanning rate of 50 mV s^{-1} (Fig. S9†). The current densities and the E_{pp} value of NiS_2 MSs CE have nearly no change during 100 cycles, while the E_{pp} of Pt CE increases noticeably. Moreover, symmetrical dummy cells (CE/electrolyte/CE) were also subjected to sequential scanning of EIS for 10 cycles (Fig. S10†). There were no obvious changes in both R_s and Z_N for all CEs, suggesting that the potential cycling exerted negligible influence on the series resistance as well as the mass transport between the CEs and redox pairs. The R_{ct} for Pt CE increased from 0.92 Ω cm^2 in the first cycle to 1.31 Ω cm^2 in the final cycle. However, for the NiS_2 MSs CE, the R_{ct} kept nearly constant (increasing from 0.76 to 0.81 Ω cm^2). These electrochemical characterization confirmed that the NiS_2 MSs CE had better electrochemical stability than that of Pt CE in iodine electrolyte.[54] This result also implied that the NiS_2 MSs CE had better corrosion resistance to the iodine-based electrolyte than Pt CE.

4. Conclusion

In summary, 3D hierarchical NiS_2 microspheres had been prepared through a facile chemical etching/anion exchange reaction followed by a controlled annealing treatment. The as-prepared NiS_2 hierarchical microspheres were constructed by 2D nanoflakes building blocks, and possessed large surface areas, high structural void porosity and accessible inner

surface. All of these features were beneficial for the mass diffusion and fast charge transport between electrolyte and CEs. A series of chemical characterization, including CV, EIS and Tafel-polarization, showed that the resultant NiS_2 hierarchical microspheres had excellent electrocatalytic activity and stability toward the reduction of I_3^- ions. A typical device assembled with NiS_2 hierarchical microspheres achieved an impressive PCE of 8.46% under AM1.5G illumination, higher that of pyrolysis Pt electrodes (8.05%). This strategy opened up a new way to synthesize a variety of hierarchical structures by selective etching of Prussian blue analogous.

Conflicts of interest

There are no conflicts to declare.

Acknowledgements

The work was supported by the National Natural Science Foundation of China (21601120, 11375111 and 21771124), the Project Funded by China Postdoctoral Science Foundation (2017M610244) and the Science and Technology Commission of Shanghai Municipality (17ZR1410500 and 15520720900).

Notes and references

1 B. O'Regan and M. Grätzel, *Nature*, 1991, **353**, 737–740.
2 S. N. Yun, A. Hagfeldt and T. L. Ma, *Adv. Mater.*, 2014, **26**, 6210–6237.
3 L. Kavan, *Current Opinion in Electrochemistry*, 2017, vol. 2, pp. 88–96.
4 Y. Hou, D. Wang, X. H. Yang, W. Q. Fang, B. Zhang, H. F. Wang, G. Z. Lu, P. Hu, H. J. Zhao and H. G. Yang, *Nat. Commun.*, 2013, **4**, 1583.
5 E. Olsen, G. Hagen and S. E. Lindquist, *Sol. Energy Mater. Sol. Cells*, 2000, **63**, 267–273.
6 L. Kavan, *Top. Curr. Chem.*, 2014, **348**, 53–94.
7 L. Kavan, J. H. Yum and M. Graetzel, *Electrochim. Acta*, 2014, **128**, 349–359.
8 M. Janani, P. Srikrishnarka, S. V. Nair and A. S. Nair, *J. Mater. Chem. A*, 2015, **3**, 17914–17938.
9 L. Kavan, P. Liska, S. M. Zakeeruddin and M. Gratzel, *Electrochim. Acta*, 2016, **195**, 34–42.
10 T. H. Lee, K. Do, Y. W. Lee, S. S. Jeon, C. Kim, J. Ko and S. S. Im, *J. Mater. Chem.*, 2012, **22**, 21624–21629.
11 R. Trevisan, M. Dobbelin, P. P. Boix, E. M. Barea, R. Tena-Zaera, I. Mora-Sero and J. Bisquert, *Adv. Energy Mater.*, 2011, **1**, 781–784.
12 Q. W. Tang, Y. Y. Duan, B. L. He and H. Y. Chen, *Angew. Chem., Int. Ed.*, 2016, **55**, 14410–14414.
13 X. X. Chen, Q. W. Tang, B. L. He, L. Lin and L. M. Yu, *Angew. Chem., Int. Ed.*, 2014, **53**, 10799–10803.
14 X. W. Wang, Y. Xie, B. Bateer, K. Pan, Y. T. Zhou, Y. Zhang, G. F. Wang, W. Zhou and H. G. Fu, *Nano Res.*, 2016, **9**, 2862–2874.
15 F. Gong, H. Wang, X. Xu, G. Zhou and Z. S. Wang, *J. Am. Chem. Soc.*, 2012, **134**, 10953–10958.
16 J. Yang, C. X. Bao, K. Zhu, T. Yu, F. M. Li, J. G. Liu, Z. S. Li and Z. G. Zou, *Chem. Commun.*, 2014, **50**, 4824–4826.
17 Y. M. Xiao, G. Y. Han, H. H. Zhou, Y. P. Li and J. Y. Lin, *Electrochim. Acta*, 2015, **155**, 103–109.
18 Y. M. Xiao, J. H. Wu, J. Y. Lin, G. T. Yue, J. M. Lin, M. L. Huang, Y. F. Huang, Z. Lan and L. Q. Fan, *J. Mater. Chem. A*, 2013, **1**, 13885–13889.
19 Z. Q. Wan, C. Y. Jia and Y. Wang, *Nanoscale*, 2015, **7**, 12737–12742.
20 J. L. Zheng, W. Zhou, Y. R. Ma, W. Cao, C. B. Wang and L. Guo, *Chem. Commun.*, 2015, **51**, 12863–12866.
21 Y. P. Liao, K. Pan, Q. J. Pan, G. F. Wang, W. Zhou and H. G. Fu, *Nanoscale*, 2015, **7**, 1623–1626.
22 X. Huang, C. L. Tan, Z. Y. Yin and H. Zhang, *Adv. Mater.*, 2014, **26**, 2185–2204.
23 Y. Q. Zhu, C. B. Cao, S. Tao, W. S. Chu, Z. Y. Wu and Y. D. Li, *Sci. Rep.*, 2014, **4**, 5787.
24 S. Wan, J. Qi, W. Zhang, W. Wang, S. Zhang, K. Liu, H. Zheng, J. Sun, S. Wang and R. Cao, *Adv. Mater.*, 2017, **29**, 1700286.
25 S. S. Huang, Q. Q. He, W. L. Chen, J. T. Zai, Q. Q. Qiao and X. F. Qian, *Nano Energy*, 2015, **15**, 205–215.
26 Z. Y. Dai, X. X. Zang, J. Yang, C. C. Sun, W. L. Si, W. Huang and X. C. Dong, *ACS Appl. Mater. Interfaces*, 2015, **7**, 25396–25401.
27 C. Z. Zhu, Z. F. Jiang, L. L. Chen, K. Qian and J. M. Xie, *Nanotechnology*, 2017, **28**, 115708.
28 B. You and Y. J. Sun, *Adv. Energy Mater.*, 2016, **6**, 1502333.
29 X. Y. Yu, L. Yu, B. H. Wu and X. W. Lou, *Angew. Chem., Int. Ed.*, 2015, **54**, 5331–5335.
30 L. Han, T. W. Yu, W. Lei, W. W. Liu, K. Feng, Y. L. Ding, G. P. Jiang, P. Xu and Z. W. Chen, *J. Mater. Chem. A*, 2017, **5**, 16568–16572.
31 L. Han, X. Y. Yu and X. W. Lou, *Adv. Mater.*, 2016, **28**, 4601–4605.
32 M. Hu, S. Ishihara, K. Ariga, M. Imura and Y. Yamauchi, *Chem.–Eur. J.*, 2013, **19**, 1882–1885.
33 J. T. Zai, X. F. Qian, K. X. Wang, C. Yu, L. Q. Tao, Y. L. Xiao and J. S. Chen, *CrystEngComm*, 2012, **14**, 1364–1375.
34 A. Amrani, A. Kamyshny, O. Lev and Z. Aizenshtat, *Inorg. Chem.*, 2006, **45**, 1427–1429.
35 X. H. Xia, C. R. Zhu, J. S. Luo, Z. Y. Zeng, C. Guan, C. F. Ng, H. Zhang and H. J. Fan, *Small*, 2014, **10**, 766–773.
36 X. Qian, H. M. Li, L. Shao, X. C. Jiang and L. X. Hou, *ACS Appl. Mater. Interfaces*, 2016, **8**, 29486–29495.
37 C. Q. Wang, B. Tian, M. Wu and J. H. Wang, *ACS Appl. Mater. Interfaces*, 2017, **9**, 7084–7090.
38 T. C. An, Y. Wang, J. Tang, W. Wei, X. Q. Cui, A. M. Alenizi, L. J. Zhang and G. F. Zheng, *J. Mater. Chem. A*, 2016, **4**, 13439–13443.
39 B. C. Qiu, Q. H. Zhu, M. M. Du, L. G. Fan, M. Y. Xing and J. L. Zhang, *Angew. Chem., Int. Ed.*, 2017, **129**, 2728–2732.
40 P. J. Li and Q. W. Tang, *J. Power Sources*, 2016, **317**, 43–48.
41 K. Mokurala, S. Mallick and P. Bhargava, *J. Power Sources*, 2016, **305**, 134–143.

42 M. X. Wu, J. Bai, Y. D. Wang, A. J. Wang, X. Lin, L. Wang, Y. H. Shen, Z. Q. Wang, A. Hagfeldt and T. L. Ma, *J. Mater. Chem.*, 2012, **22**, 11121–11127.
43 J. D. Roy-Mayhew, D. J. Bozym, C. Punckt and I. A. Aksay, *ACS Nano*, 2010, **4**, 6203–6211.
44 Z. Q. Li, F. Gong, G. Zhou and Z. S. Wang, *J. Phys. Chem. C*, 2013, **117**, 6561–6566.
45 W. J. Wang, X. Pan, W. Q. Liu, B. Zhang, H. W. Chen, X. Q. Fang, J. X. Yao and S. Y. Dai, *Chem. Commun.*, 2014, **50**, 2618–2620.
46 J. H. Guo, Y. T. Shi, C. Zhu, L. Wang, N. Wang and T. L. Ma, *J. Mater. Chem. A*, 2013, **1**, 11874–11879.
47 V. D. Dao, L. L. Larina, J. K. Lee, K. D. Jung, B. T. Huy and H. S. Choi, *Carbon*, 2015, **81**, 710–719.
48 L. Kavan, H. Krysova, P. Janda, H. Tarabkova, Y. Saygili, M. Freitag, S. M. Zakeeruddin, A. Hagfeldt and M. Gratzel, *Electrochim. Acta*, 2017, **251**, 167–175.
49 V. D. Dao, S. H. Jung, J. S. Kim, Q. C. Tran, S. A. Chong, L. L. Larina and H. S. Choi, *Electrochim. Acta*, 2015, **156**, 138–146.
50 G. Yue, J. Wu, J.-Y. Lin, Y. Xiao, S.-Y. Tai, J. Lin, M. Huang and Z. Lan, *Carbon*, 2013, **55**, 1–9.
51 Y. J. Li, Q. W. Tang, L. M. Yu, X. F. Yan and L. Dong, *J. Power Sources*, 2016, **305**, 217–224.
52 M. X. Wu, X. Lin, Y. D. Wang, L. Wang, W. Guo, D. D. Qu, X. J. Peng, A. Hagfeldt, M. Gratzel and T. L. Ma, *J. Am. Chem. Soc.*, 2012, **134**, 3419–3428.
53 F. N. Pardo, D. Benetti, H. G. Zhao, V. M. Castano, A. Vomiero and F. Rosei, *J. Power Sources*, 2016, **335**, 138–145.
54 Y. C. Wang, D. Y. Wang, Y. T. Jiang, H. A. Chen, C. C. Chen, K. C. Ho, H. L. Chou and C. W. Chen, *Angew. Chem., Int. Ed.*, 2013, **52**, 6694–6698.